Applied Surface Science 360 (2016) 461–469

Contents lists available at ScienceDirect

Applied Surface Science

journal homepage: www.elsevier.com/locate/apsusc

Effects of sintering and mixed oxide growth on the interface cracking of air-plasma-sprayed thermal barrier coating system at high temperature

Bowen Lv[a], Hua Xie[b], Rong Xu[a], Xueling Fan[a], Weixu Zhang[a,*], T.J. Wang[a]

[a] State Key Laboratory for Strength and Vibration of Mechanical Structures, School of Aerospace Engineering, Xi'an Jiaotong University, Xi'an 710049, PR China

[b] State Key Laboratory for Mechanical Behavior of Materials, School of Materials Science and Engineering, Xi'an Jiaotong University, Xi'an, Shaanxi 710049, PR China

ARTICLE INFO

Article history:
Received 9 August 2015
Received in revised form
29 September 2015
Accepted 6 October 2015
Available online 9 October 2015

Keywords:
Thermal barrier coating
Sintering
Mixed oxide
Interface crack
Constitutive model
Finite element method

ABSTRACT

Sintering and mixed oxide (MO) growth significantly affect the thermal and mechanical properties of thermal barrier coating system (TBCs) in gas turbine at high temperature. In this work, we numerically analyzed the effects of sintering and MO growth on the interface cracking of TBCs. A thermal-elasto-viscoplastic constitutive model was introduced, in which the effect of sintering was studied using a spherical shell model. Based on the same spherical shell model and our previous experimental observations, we theoretically derived the evolution of relative density and applied this constitutive model to the sintering of ceramic coating. The numerical results showed that viscosity, initial porosity of ceramic and the growth rate of MO had significant effects on interface cracking. In contrast, the influence of initial pore size of ceramic coating was neglectable. Suggestions were also made for the choice of material during TBCs design.

1. Introduction

The increase of inlet gas temperature is one way to improve the performance of gas turbine. Thermal barrier coating system (TBCs) provides thermal protection and oxidation insulation for the elements working at high temperature. The air plasma sprayed (APS) technology is employed to manufacture the TBCs in the industrial gas turbine for power generation [1]. APS-TBCs is composed of three layers: the substrate, the bond-coat (BC), and the ceramic top coat (TC). High temperature sintering significantly affects the thermal and mechanical properties of TBCs, e.g., strain tolerance, durability and thermal insulation performance [2,3]. On the other hand, mixed oxide (MO) forms and grows at elevated temperature, which may result in the interfacial damage and speed up the debonding of coatings. Both sintering and MO growth affect the service life of TBCs.

At elevated temperature, the sintering of TC is caused by the interconnection of ceramic splats driven by surface energy, accompanying with macroscopic volumetric shrinkage. According to Coble's definition [4], sintering of solid can be divided into three stages depending on the change of pore shape. In the initial stage of sintering, neck growth leads to the increase of contact area of interparticle. The intermediate stage is characterized by the formation of equilibrium dihedral angles on the pore surface. In the final stage, pores are ultimately closed. Particularly in APS-TBCs [5,6], the first two stages are summed up to be a stage of inter-splat bonding improvement, which is dominated by surface diffusion and evaporation-condensation [7] and is relatively fast (<10 h). In the second quasi-stationary stage, macro-pore shrinks and tends to be more spherical. The later stage is dominated by sintering stress coming from surface energy [8,9] and is relatively long. Considering the long-term service of industrial gas turbine, sintering in the later stage is more crucial to the performance and lifetime of APS-TBCs, which attracts great interest in understanding the effect of sintering on APS-TBCs.

Theoretical and experimental investigations have been carried out to understand the effect of sintering. However, restricted by experimental conditions, limited parameters are considered in analysis, e.g. elastic modulus, thermal conductivity, diffusivity, porosity and impurity [6,10–12]. Besides, Ahrens et al. [13]

* Corresponding author.
E-mail address: zhangwx@mail.xjtu.edu.cn (W. Zhang).

http://dx.doi.org/10.1016/j.apsusc.2015.10.037
0169-4332/

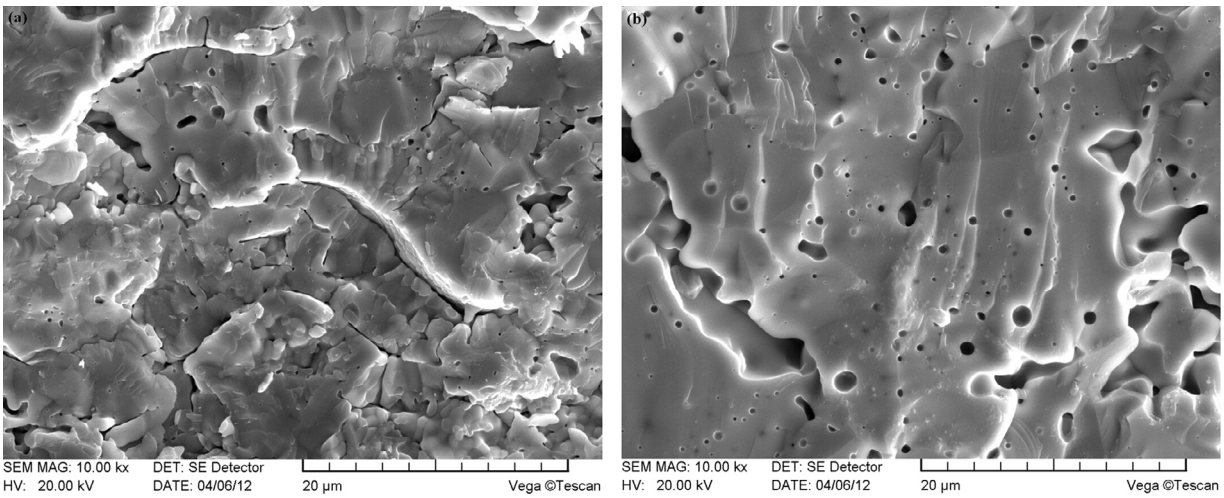

Fig. 1. Cross-sectional microstructure of TBCs sintered at 1300 °C for (a) 50 h and (b) 500 h.

observed the time-dependent deformation behavior in a series of in situ three-point bending tests at different annealing temperatures. Based on variational principle, Cipitria et al. [14,15] proposed a sintering model and predicted the evolution of microstructure in TBCs. Fleck and Cocks [16] developed a constitutive model for TBCs incorporating the elastic response, local contact problem, sintering, diffusion and creep behaviors. They used a brick model for TBCs to study the sintering of splats [17]. However, the effect of sintering on the interface cracking has not been reported to the best of our knowledge.

MO growth is one of the major factors affecting interface cracking of TBCs. In the early service stage of TBCs, the thermally grown oxide (TGO) is mainly dense and uniform α-Al_2O_3. Then, MO (i.e. NiO, Cr_2O_3 and spinel) forms. The main reason of MO formation is the depletion of aluminum [18] or the depletion of Al_2O_3 [19]. The growth rate of MO is fast, typically three orders higher than that of α-Al_2O_3, and is approximately linear in time. More importantly, due to its porous and nonuniform features, MO may result in the concentration of local stress, interface damage and significant reduction of interface strength.

In the last decades, investigations concern the effect of TGO on the failure of TBCs, for example the effect of TGO on the stress distribution and interface morphology [20–26]. Also, attentions have been devoted to the effect of MO on the failure of TBCs [18,27]. Relatively, numerical analysis is not so much, e.g. Xu et al. [28] investigated the effects of MO spacing and its growth rate on interface cracking via finite element method, in which the effect of sintering is not considered.

The motivation of this work is to study the effects of sintering and MO growth on the interface cracking of TBCs at high temperature. In Section 2, the problem is stated, including constitutive models for sintering and MO growth. In Section 3, a finite element model is constructed based on typical TBCs structures, taking both sintering and MO growth into consideration. In Section 4, the effects of material and microstructural parameters are discussed in detail. Conclusions are drawn in Section 5.

2. Statement of the problem

2.1. Experimental observations

A detailed examination of the microstructure evolution was carried out for the comprehension of whole sintering process [29]. Coating material is 20 wt% yttria stabilized zirconia (YSZ) powder (Xiandao, Yiyang, China) from 30 μm to 70 μm in size with a mean value of 47 μm. Stainless steel substrates were employed for the deposition of YSZ coatings. We obtained the freestanding coatings by dissolving the substrate in hydrochloric acid. The 20 wt% YSZ coating underwent heat treatment at 1300 °C for different durations from 50 h to 500 h. Cross-sectional microstructures were analyzed by using scanning electron microscope (SEM) before and after high temperature exposure. Statistical data of apparent porosity of the coatings were obtained through image analysis. The apparent porosity decreased during sintering, especially in the early 50 h. For the purpose of revealing microstructural evolution, we examined the fractured cross-sectional morphologies of annealed coatings. The typical lamellar structure tended to disappear during sintering. Healing of intersplat microcracks and spheroidization of pores were observed during sintering, as shown in Fig. 1(a) and (b).

The effect of MO growth on the interfacial delamination was studied in our previous experiment [18]. TC was prepared by APS method with 8YSZ powder (Metco 204B-NS, Sulzer Metco Inc., New York, USA). BC was deposited by a cold spray system with NiCoCrAlTaY powder (Amdry 997, Sulzer Metco Inc., New York, USA). The substrate was nickel-based superalloy (Mar-M247). As-sprayed TBCs went through heat treatment to introduce TGOs including MO to the interface between TC and BC. SEM (VEGA II-XMU, TESCAN, Czech) was employed for the observation of MO. The MO composed of spinel and NiO/Cr_2O_3 presented at the interface exhibiting protrusion morphology due to much faster growth than α-Al_2O_3. The protrusion expanded and induced interfacial delamination with the growth of MO, as shown in Fig. 2.

2.2. Constitutive model for the sintering of TBCs

The TC of as-sprayed TBCs has a lamellar microstructure with random distributed pores and cracks. After heat treatment, the splats of TC sinter together accompanying with microcrack healing and pore spheroidization, which is confirmed by our experiment in Section 2.1 (see Fig. 1(a) and (b)). Therefore, the microstructure of sintered TBCs can be regarded as a homogeneous material with random spherical pores shown in Fig. 3(a). With the process of sintering, these pores tend to be homogenized (Fig. 3(b)). Keeping the same volume fraction, these cells can be equivalent to a representative volumetric element (RVE) of a spherical shell, as shown in Fig. 3(c), which has been proved applicable [30]. Based on the above simplification, we use a thermo-elasto-viscoplastic

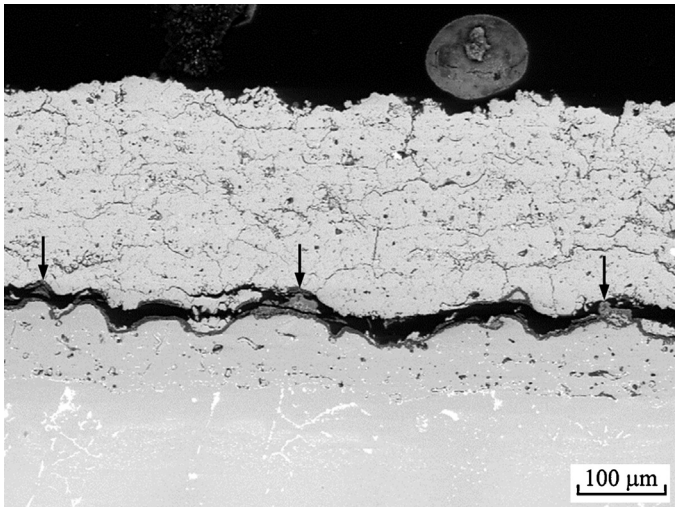

Fig. 2. Cross-sectional microstructure of MO (pointed out by black arrows) at the interface inducing delamination.

constitutive model developed by Gasik and Zhang [31] and Shinagawa [32]. Note that micro-cracks in the TBCs tend to be healed during sintering and lamellar pores become nearly spherical as well [6,10,33,34]. Therefore, it is reasonable to treat the whole TC as a homogeneous material distributed with uniform spherical pores at annealing temperature and apply Gasik–Zhang constitutive model to study the sintering effect on TBCs. Note that the proposed constitutive model can only be applied to the macroscopic sintering due to the simplification mentioned above. Prediction of the microstructural evolution induced by sintering requires modification in the derivation of sintering stress in the constitutive model.

The mechanical behavior of TBCs at high temperature is mainly controlled by four factors: elastic deformation, sintering shrinkage, viscoplastic creep, and thermal expansion, as schematically shown in Fig. 4 [31]. This relationship can be described by the following incremental equation [31]:

$$\{d\varepsilon\} = \{d\varepsilon^E\} + \{d\varepsilon^{Vp}\} + \{d\varepsilon^{sint}\} + \{d(\alpha T)\}, \quad (1)$$

with $d\varepsilon$ being the total strain increment, $d\varepsilon^E$ being the elastic strain increment, $d\varepsilon^{Vp}$ being the viscous plastic strain increment, $d\varepsilon^{sint}$ being the free sintering volumetric strain increment, and $d(\alpha T)$ being the thermal strain increment. These strain increments follow Gasik–Zhang derivation [31]. The constitutive equation is presented as follows:

$$\{d\sigma\} = [D^*]\left(\{d\varepsilon\} - [\eta]^{-1}\{\sigma\}dt - \{d\varepsilon^{sint}\} - d\{\alpha T\}\right), \quad (2)$$

where modified elastic matrix $[D^*] = \left([I] + 1/2[D][\eta]^{-1}\{\sigma\}dt\right)^{-1}[D]$ with $[I]$ being the identity matrix, $[\eta]$ being the viscous matrix

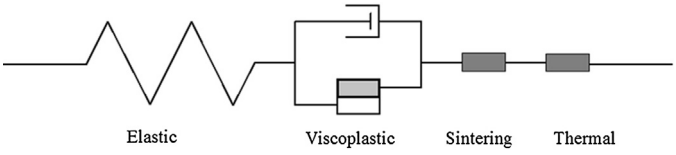

Fig. 4. Four main factors controlling the sintering process of TBCs at high temperature.

according to Gasik and Zhang [31], and $[D]$ being the elastic matrix. In addition, $[D]$ can be written as

$$[D] = \frac{E}{1+\nu}\begin{bmatrix} \frac{1-\nu}{1-2\nu} & \frac{\nu}{1-2\nu} & \frac{\nu}{1-2\nu} & 0 & 0 & 0 \\ \frac{\nu}{1-2\nu} & \frac{1-\nu}{1-2\nu} & \frac{\nu}{1-2\nu} & 0 & 0 & 0 \\ \frac{\nu}{1-2\nu} & \frac{\nu}{1-2\nu} & \frac{1-\nu}{1-2\nu} & 0 & 0 & 0 \\ 0 & 0 & 0 & \frac{1}{2} & 0 & 0 \\ 0 & 0 & 0 & 0 & \frac{1}{2} & 0 \\ 0 & 0 & 0 & 0 & 0 & \frac{1}{2} \end{bmatrix}, \quad (3)$$

where E is the Young's modulus and ν is the Poisson's ratio.

As sintering proceeds, the volume reduction of pores leads to global shrinkage of ceramics and the increase of density. It is seen that relative density is related to most parameters in the constitutive equations. Therefore, it is necessary to study the variation of density against sintering time. Using a CCD camera with post-treatment on a computer, Gasik and Zhang [31] obtained the time-history curve of relative density. Here, we theoretically investigate its evolution by the spherical shell model (Fig. 3(c)) introduced by Shinagawa [32] to deduce shrinkage rate and sintering stress.

We derived the relationship between relative density ρ and sintering time t based on mass conservation, geometric relation and mechanical relation (see Appendix A for detail). The relationship is expressed as follows:

$$t = -\frac{2}{3}\left(\frac{\rho_0}{1-\rho_0}\right)^{1/3}\frac{\eta k R_0}{\gamma}\int_{\rho_0}^{\rho}(1-\rho)^{-2/3}\rho^{-11/3}d\rho, \quad (4)$$

Though sintering temperature influences the relative density, in the present study, its influence is fixed since only constant temperature is considered.

2.3. MO growth

Experiments [18,19] show that MO grows at approximately constant rate at elevated temperature. For the plane strain problem, MO growth can be described by two independent parameters in orthogonal directions. Two growth rate factors are chosen: $g_\perp$ is for

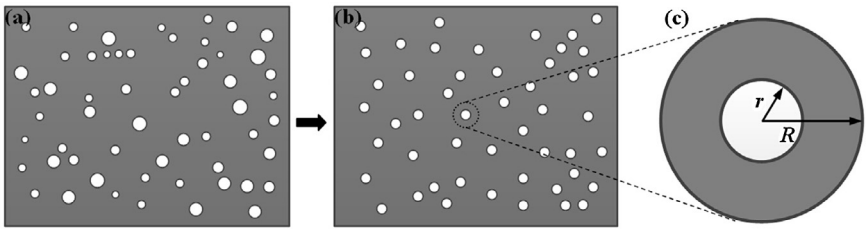

Fig. 3. Simplification of microstructure from experimental observed real structure to (a) idealized homogenous structure with random distributed pores; (b) structure with homogenous pores; (c) representative volumetric element of spherical shell structure.

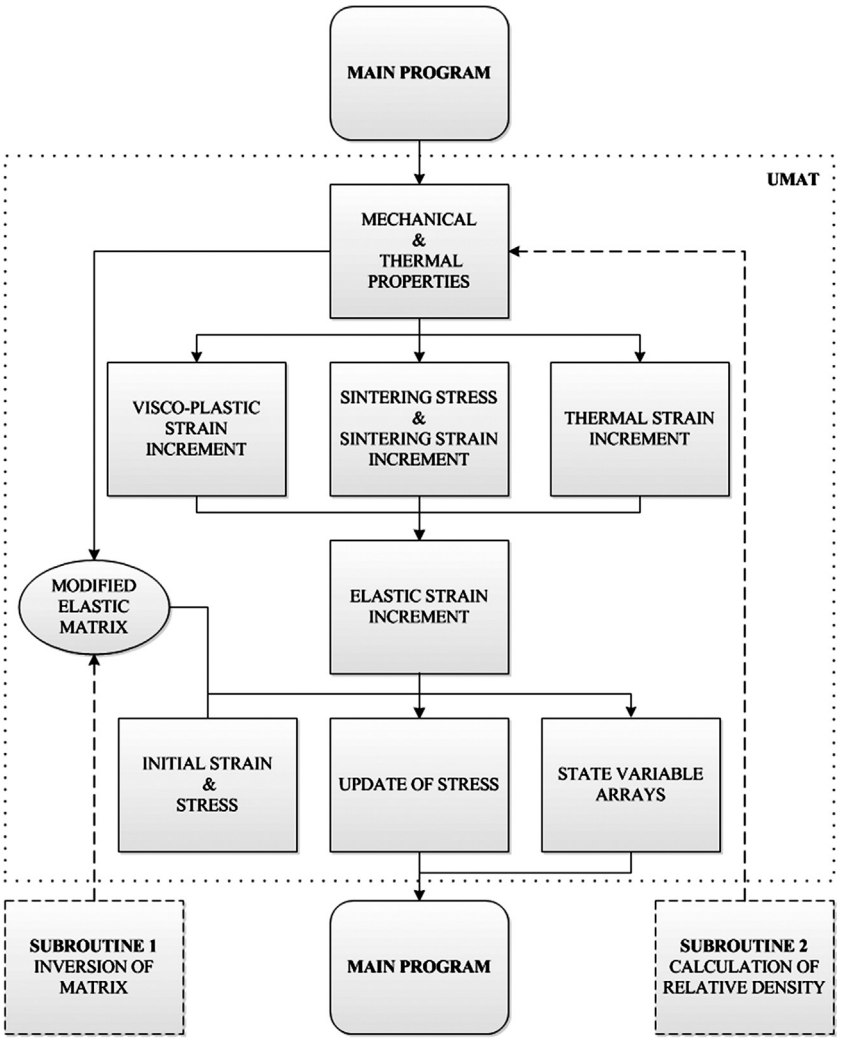

Fig. 5. Flow chart of FE analysis with user subroutine UMAT.

the growth rate perpendicular to the interface and $g_{\parallel}$ is the parallel one. In consequence, the strain variation induced by the thermal growth of MO can be expressed in the corresponding directions as follows:

$$\Delta\varepsilon_{\perp}^{g} = g_{\perp}\mathrm{d}t \tag{5}$$

$$\Delta\varepsilon_{\parallel}^{g} = g_{\parallel}\mathrm{d}t \tag{6}$$

3. Finite element analysis

To highlight the TC–BC interface with MO growth, TBCs can be simplified as a two-layer system. A 2D plane strain problem is extracted as shown in Fig. 6. MO is represented by the repetitive periodic semi-circles for simplification. Other components of TGO (mainly α-Al_2O_3) are represented by a thin layer between MO and BC. Geometry parameters are listed in Table 1. Properties of the materials can be found in Table 2. The sintering behavior of TC is described by the constitutive model stated in Section 2.2 with viscosity of 10 GPah [13,35], initial porosity of 14% [36] and initial pore size of 1 μm [37,38]. We implement the sintering constitutive model into ABAQUS with a user subroutine UMAT. The flow chat of the implementation is presented in Fig. 5. BC and substrate are considered to be linear elastic. In the initial stage of oxidation, α-Al_2O_3 appears first as a preferred oxidation-insulating layer. The growth

Table 1
Geometry parameters of FE model.

Geometry parameters	Value (μm)
Thickness of TC	200
Thickness of TGO	1
Thickness of BC	29
Thickness of substrate	470
Radius of MO	5
Width of model	50

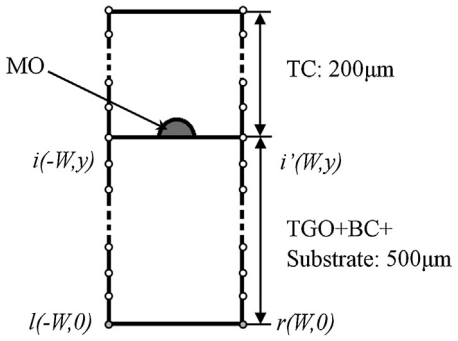

Fig. 6. Schematic model of TBCs with MO at the interface between TC and BC; nodes marked for the application of periodic boundary condition.

Table 2
Material properties of TBCs.

	TC	MO	TGO	BC + substrate
Young's modulus/GPa	$219 \times e^{-8\times(1-\rho)}$ [11,31,43]	100 [28]	350 [28]	210 [28]
Poisson's ratio	0.18 [44]	0.3 [28]	0.3 [28]	0.3 [28]
Expansion coefficient	10^{-5} [44]	0.8×10^{-5} [28]	0.9×10^{-5} [28]	1.5×10^{-5} [28]

rate of α-Al_2O_3 is slow and parabolic. After a period of service, Al depletes and then MO forms. Its growth rate is significantly higher than that of α-Al_2O_3 and approximately linear, set to be vertically 0.01 h^{-1} and horizontally 0.005 h^{-1} [28]. Here, the growth of α-Al_2O_3 is ignored comparing with that of MO. The growth of MO is written into ABAQUS via a user subroutine UEXPAN.

The meshes are shown in Fig. 7, in which those near the interface are carefully refined. The 4-node bilinear plane strain elements are employed in the quad-dominated shape. The periodic boundary conditions are applied to the left and right edges of the model, which is realized by a series of constraint equations [39,40] related to reference points (node l and node r) and the corresponding nodes on both boundaries (node i and node i') shown in Fig. 6. With the consideration of periodicity, their coordinates satisfy the following relations,

$$\begin{cases} x_i(W,y) - x_l(W,0) = x_{i'}(-W,y) - x_r(-W,0) \\ y_i(W,y) - y_l(W,0) = y_{i'}(-W,y) - y_r(-W,0) \end{cases} \quad (7)$$

As a result, their displacement satisfies similar relations,

$$\begin{cases} u_i(-W,y) - u_{i'}(W,y) = u_l(-W,0) - u_r(W,0) \\ v_i(-W,y) - v_{i'}(W,y) = v_l(-W,0) - v_r(W,0) \end{cases} \quad (8)$$

The upper boundary is free. On the lower boundary, the vertical displacement is fixed and the horizontal one is free. A constant temperature of 1473 K is applied throughout the model as thermal boundary condition. No mechanical force is exerted to this model.

The "Debond" technique [41] is adopted here to simulate the initiation and propagation of interface crack between TC and BC. The following critical stress criterion is chosen to predict the initiation of interfacial delamination:

$$f = \sqrt{\left(\frac{\hat{\sigma}_n}{\sigma^f}\right)^2 + \left(\frac{\tau_1}{\tau_1^f}\right)^2 + \left(\frac{\tau_2}{\tau_2^f}\right)^2}, \quad \hat{\sigma}_n = \max(\sigma_n, 0) \quad (9)$$

where σ_n is the normal component of stress carried across the interface at a specified distance (Fig. 8), τ_1 and τ_2 are the shear stress components in the interface, σ^f and τ^f are the normal and shear failure stresses, which should be experimentally obtained and must be specified in analysis. For the present plane strain problem, the shear stress $\tau_2 = 0$ and τ_1 is negligible over the normal stress. The crack-tip node debonds when the fracture parameter f reaches the value 1.0 with the critical normal stress of 150 MPa [28].

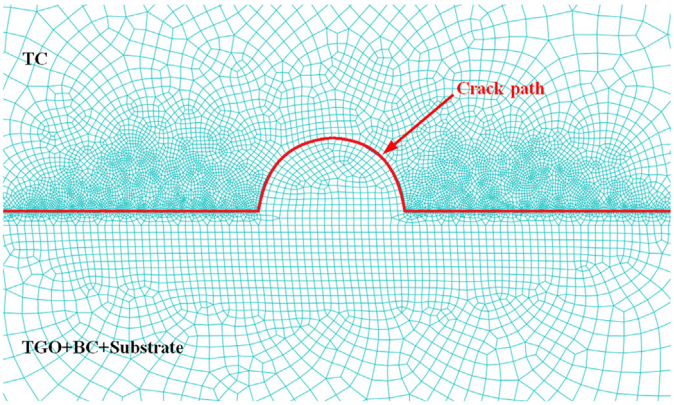

Fig. 7. FE model of TBCs with refined meshes near the interface.

4. Results and discussion

Sintering of TBCs at high temperature is related to several material parameters in the constitutive model stated in Section 2.2. In order to investigate the effect of sintering, it is more transparent to elucidate separately the effect of each material parameter. Taking the effect of sintering into consideration, the interfacial cracking induced by MO growth may be different from that in our previous work [28]. Consequently, the interfacial delamination of TBCs needs to be further discussed. In the following discussion, a referential calculation was first carried out with fixed parameters (η_0 = 10 GPah, ρ_0 = 0.86, r_0 = 1 μm and g_0 = 0.01 h^{-1}). Then a single parameter was taken as a variable to reveal its effect.

4.1. The effect of sintering of TBCs

4.1.1. Viscosity

Viscosity is a key parameter controlling the sintering process. To get a better understanding of the relationship between the viscosity and interface crack propagation, a series of viscosity values from $0.5\eta_0$ to $2\eta_0$ were given to TC (see Fig. 9). Note that lower viscosity value denotes a more viscous material. The crack length was normalized by the maximum value at final spallation and the time was normalized by that in the case of elastic TC. In the case of $\eta \geq \eta_0$, three typical stages of crack growth can be clearly recognized as an initiation stage, a steady propagation stage in the middle and a fast propagation stage until the final spallation. In contrast, for $\eta < \eta_0$, no spallation is observed in the range of calculation time.

Generally speaking, lower viscosity value of TC leads to stress relaxation and is preferred for improving the durability of TBCs. Viscosity has significant effect on the propagation of interface crack while the initiation stage is slightly affected. On one hand, the propagation tends to stop under a certain viscosity value. On the other hand, the final spallation time tends to approach 1.0 with viscosity value increasing. This tendency indicates that the debonding of a high-viscosity TC can be degenerated to the situation of the elastic one.

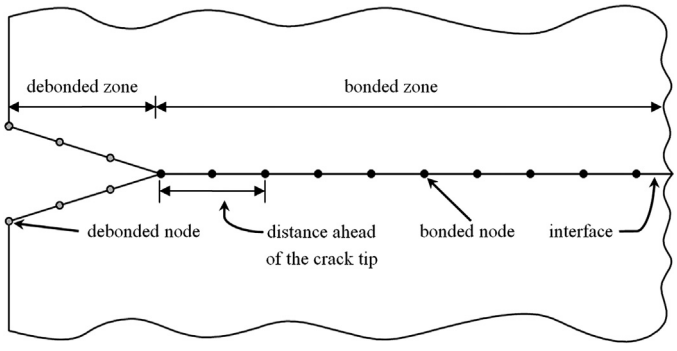

Fig. 8. The "Debond" technique for the simulation of interface crack initiation and propagation.

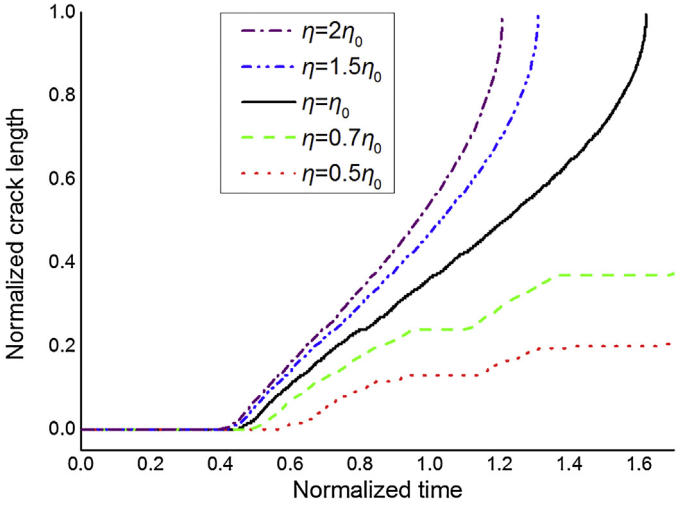

Fig. 9. Interface crack propagation with different viscosities (η) of TC: the propagation slows down with more viscous TC (lower viscosity value).

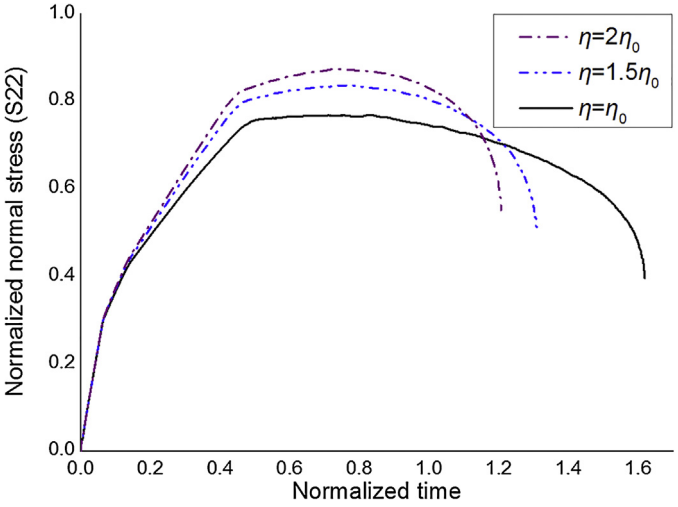

Fig. 11. Time history curve of normal stress (S_{22}) at Point D in the cases of different viscosities (η): lower normal stress after crack initiation with more viscous TC (lower viscosity value).

The above tendency can be explained by the stress state in TBCs (Fig. 10). Only the normal stress S_{22} is shown in the cloud chart, as the in-plane stress S_{11} and shear stress S_{12} are neglectable compared to S_{22}. Caused by the growth of MO, a tensile area (Zone A) can be found below the MO. Just around this area, a compressive area (Zone B) forms due to the constraint of TC. Along with crack propagation, stress concentration can be observed at the crack tip (Zone C). In these three representative zones of stress state, point D situates on the interface of TC and MO, which makes it a characteristic point for stress analysis. Since the stress distribution patterns are almost the same for all the cases studied herein, only the normal stress (S_{22}) of point D will be extracted and examined in the following discussion. In addition, only time history curves for $\eta \geq \eta_0$ are shown.

It is seen from Fig. 11 that the more viscous the material is, the lower the normal stress becomes, which slows interface crack propagation as stated above. Furthermore, no obvious change in the stress state is observed until the moment ($t = 0.2$) close to crack initiation ($t = 0.4$), which indicates that the change of viscosity has a relatively little effect on the stress state at early stage. In other words, it has little effect on the crack initiation, as shown in Fig. 9.

4.1.2. Initial porosity

The effect of porosity on sintering can be revealed by studying the effect of relative density. Along with the sintering process, microcrack closure takes place and the volume of pores reduces driven by sintering stress. It is shown that the relative density of sintered TBCs can increase from 0.86 to 0.95 or even higher [1,36,38]. In this work, five groups of initial relative density are taken into consideration. Fig. 12 shows interface cracking for the cases of $\rho \geq \rho_0$. In these cases, the more porous the TC material is, the better crack resistance the interface has. Both the crack initiation and the final debonding moments are significantly affected by the change of relative density. It appears that the effect becomes more significant as the relative density decreases. For example, the crack initiation and spallation are retarded by 22.3% and 26.2%, respectively, when the initial relative density declines from 0.96 to 0.91; they are retarded by 25.7% and 38.5% when the density changes from 0.91 to 0.86. These data also show that the final spallation of coating is more sensitive to porosity compared to the crack initiation. It should be noted that cracking is not observed for $\rho < \rho_0$. One reason could be attributed to the relaxation. In numerical analysis, fracture is governed by the stress state (see Section 3). Materials with lower density release more energy. Consequently, crack initiation can hardly be triggered in these cases.

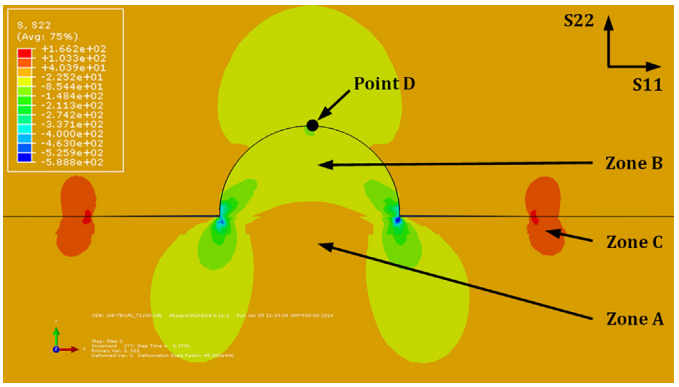

Fig. 10. Cloud chart of the normal stress distribution (S_{22}) around interface crack: a tensile area (Zone A) caused by MO growth; a compressive area (Zone B) because of the constraint by TC; stress concentration at the crack tip (Zone C); a characteristic point (Point D) for stress evaluation on the interface of TC and MO.

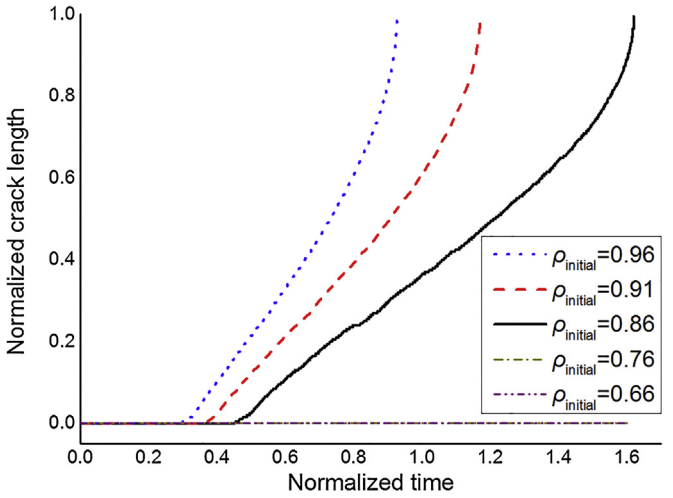

Fig. 12. Interface crack propagation with different initial relative densities ($\rho_{initial}$) of TC: the initiation retards and propagation slows down with more porous TC (lower initial relative density).

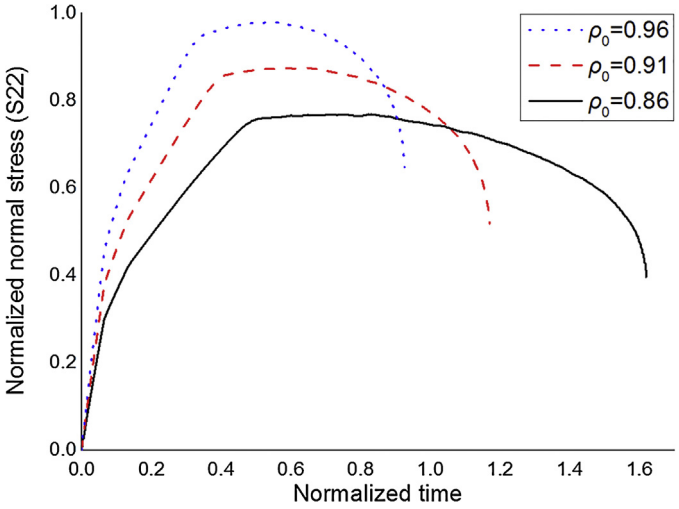

Fig. 13. Time history curve of normal stress (S_{22}) at Point D in the cases of different initial relative densities ($\rho_{initial}$): lower normal stress since crack initiation with more porous TC (lower initial relative density).

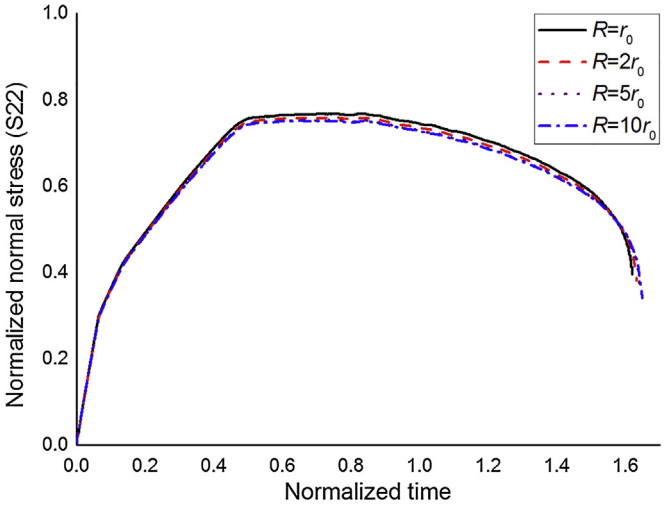

Fig. 15. Time history curve of normal stress (S_{22}) at Point D in the cases of different initial pore sizes (R): slightly lower normal stress for TC with larger pores.

The evolution of normal stress (S_{22}) at the characteristic point (Point D) is plotted in Fig. 13. It is clear that higher relative density leads to a higher normal stress and a faster sintering. As relative density increases toward 1.0, which means few pores exist in the material the behavior of porous material approaches to that of a dense elastic material. Thus, a limit (1.0) of normal stress level exists. Furthermore, changes in relative density have a remarkable effect on stress level from early stage ($t < 0.1$), which can explain the difference in crack initiation shown in Fig. 12.

In addition, the duty of TBCs is to provide thermal protection for gas turbine, which requires higher porosity for better thermal insulation ability. This requirement corresponds to the functionality of sintering resistance. Therefore, a suitable porous material for TC is recommended in the design and engineering application.

4.1.3. Initial pore size

It is known that TBCs with different pore sizes may have the same porosity. As an independent variable in the constitutive model, initial pore size may have some influence on sintering. Fig. 14 shows that initial pore size has little effect on the interface cracking. Even if the pore size becomes 10 times larger, the crack initiation and spallation are retarded by 0.7% and 1.8%, respectively. These results can be explained by the constitutive equations presented in Section 2.2. As we have discussed earlier, interface crack is driven by the sintering stress and the thermal growth of MO. For a constant growth rate, the interface crack will be governed only by the following sintering stress [31],

$$\sigma_s = \rho^N \frac{2\gamma}{kR} \left\{ \frac{\rho_{initial}(1-\rho)}{\rho(1-\rho_{initial})} \right\}^{-1/3} \tag{10}$$

where N equals to 6 according to Shinagawa's definition [32] of sintering stress.

Eq. (10) shows clearly that the importance of relative density is five orders greater than that of pore radius, which explains well the insignificant differences among the curves in Fig. 14. Consequently, the effect of pore size on interface cracking should be much smaller than that of relative density. Even though the effect of pore size is not remarkable, it still can be concluded, from Fig. 14 by comparing the spallation moment, that the smaller the pore is, the worse sintering resistance TC has. This result can be reflected by the history curve of normal stress (S_{22}) in Fig. 15 that the change in initial pore size has limited influence on it, which is also confirmed by Zhao's experiment [42].

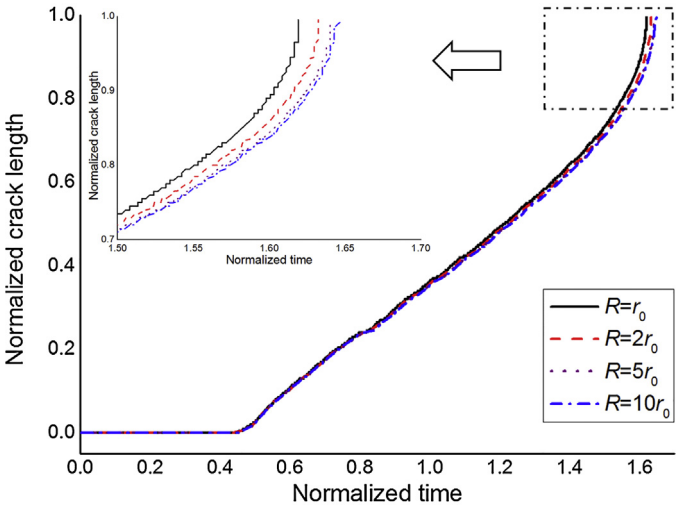

Fig. 14. Interface crack propagation with different initial pore sizes (R) of TC: the propagation slightly slows down for TC with larger pores.

4.2. The effect of MO growth

As indicated in Section 2.3, MO growth is controlled mainly by its growth rate. MO growth behavior for TBCs with elastic TC has been discussed thoroughly in the previous work by Xu et al. [28]. Here, we focus on the effect of MO growth on the interface cracking in TBCs with elasto-viscoplastic TC.

Fig. 16 shows that the initiation and propagation of interface crack are largely accelerated by higher TGO growth rate. Crack initiates 54.3% earlier and propagates 120% faster when the growth rate changes from g_0 to $2g_0$. The changes in crack initiation and propagation are 61.5% and 116%, respectively, when the growth rate increases from $2g_0$ to $5g_0$. Thus, to avoid high growth rate and to prevent interface cracking, it is of great importance to control the proportion of MO and its components. In the case of the slowest growth rate, the interface keeps well bonded within the whole range of calculation time. This result may be explained by stress relaxation as in the discussion of relative porosity. The evolution of normal stress shown in Fig. 17 explains well the significant acceleration in both crack initiation and propagation by the increase of growth rate, which is similar to those cases of different relative

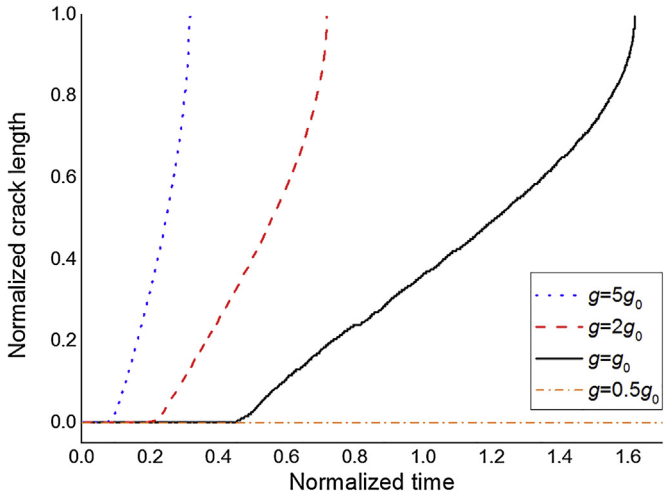

Fig. 16. Interface crack propagation with different MO growth rates (g): the initiation retards significantly and propagation slows down remarkably with slower MO growth.

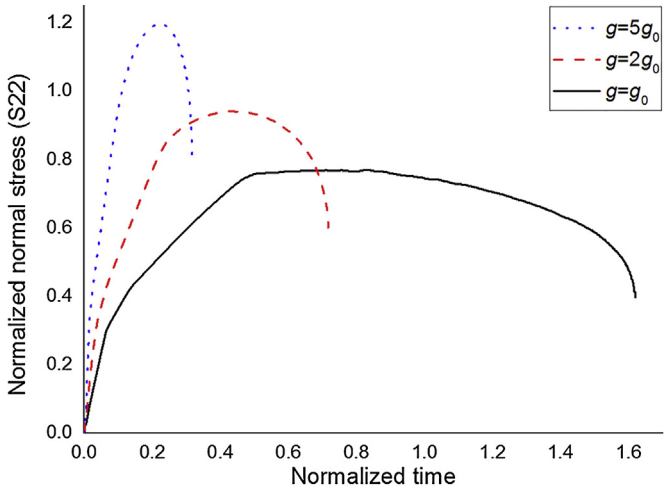

Fig. 17. Time history curve of normal stress (S_{22}) at Point D in the cases of different growth rates (g) of MO: significantly lower normal stress with slower MO growth.

densities. In the work of Xu et al. [28], limited by the elastic constitutive model of TC, cracks with different MO growth rates initiated at the same time. Thus, the effect of MO growth rate on crack initiation cannot be predicted by their model.

5. Conclusion

In this work, based on theoretically deriving the evolution of relative density during ceramic sintering at high temperature, we developed the thermo-elasto-viscoplastic constitutive model proposed by Gasik and Zhang [31]. By implementing the constitutive model into the finite element code, the effects of sintering (viscosity, initial porosity, pore radius) and mixed oxide (MO) growth on the interfacial cracking were numerically investigated. Numerical results show that viscoplasticity only slows down the propagation of interface crack but has negligible effect on the initiation of interface crack. Higher porosity and smaller MO growth rate retard both the initiation and the propagation of interface crack. Nevertheless, initial pore size has insignificant effect on the interface cracking. For the design and engineering application of thermal barrier coating system, we recommend a viscous and porous ceramic material with carefully controlled MO.

Acknowledgements

This work is supported by China 973 Program (2013CB035701), NSFC (11172227, 11472203, 11321062) and NCET (130466) and 2013GY2-14.

Appendix A. Appendix A

The density evolution of TBCs (Eq. (4)) during sintering is derived as follows. We assume that the mass of the material is invariant during sintering process. According to the mass conservation, the relationship between external radius R and internal radius r can be expressed as follows:

$$R^3 - r^3 = R_0^3 - r_0^3 \tag{A.1}$$

With the definition of relative density:

$$\rho = 1 - \left(\frac{r}{R}\right)^3 \tag{A.2}$$

We can obtain the relationship between external radius R and relative density ρ:

$$R = \left(\frac{\rho_0 R_0^3}{\rho}\right)^{1/3} \tag{A.3}$$

where R_0 and ρ_0 are initial external radius and initial relative density, respectively.

According to geometric relation, volumetric strain can be derived from external radius:

$$\varepsilon_v = 3\frac{R - R_0}{R_0} \tag{A.4}$$

With Eq. (A.3), the variational calculus of Eq. (A.4) gives:

$$\mathrm{d}\varepsilon_v = 3\frac{\mathrm{d}R}{R_0} = -\left(\frac{\rho_0}{\rho^4}\right)^{1/3}\mathrm{d}\rho \tag{A.5}$$

According to mechanical relation, the volumetric strain rate is defined by Shinagawa [32] as a function of sintering stress:

$$\dot{\varepsilon}_v = \frac{3(1-\rho)}{4\eta\rho^4}\sigma_s \tag{A.6}$$

With the sintering stress and effective pore radius given by Shinagawa [32]:

$$\sigma_s = \rho^N\frac{2\gamma}{\bar{r}} \tag{A.7}$$

$$\bar{r} = kR_0\left[\frac{\rho_0(1-\rho)}{\rho(1-\rho_0)}\right]^{1/3} \tag{A.8}$$

The variation of volumetric strain can be written as follows:

$$\mathrm{d}\varepsilon_v = \frac{3(1-\rho)}{4\eta\rho^4}\rho^6\frac{2\gamma}{kR_0}\left[\frac{\rho_0(1-\rho)}{\rho(1-\rho_0)}\right]^{-1/3}\mathrm{d}t \tag{A.9}$$

Combination of Eqs. (A.5) and (A.9) finally gives the relationship between relative density ρ and sintering time t:

$$-\frac{2}{3}\left(\frac{\rho_0^2}{1-\rho_0}\right)^{1/3}\frac{\eta k R_0}{\gamma}\int_{\rho_0}^{\rho}(1-\rho)^{-2/3}\rho^{-11/3}\mathrm{d}\rho = \int_0^t \mathrm{d}t = t \tag{A.10}$$

References

[1] N.P. Padture, M. Gell, E.H. Jordan, Thermal barrier coatings for gas-turbine engine applications, Science 296 (2002) 280–284.
[2] D. Zhu, R.A. Miller, Sintering and creep behavior of plasma-sprayed zirconia- and hafnia-based thermal barrier coatings, Surf. Coat. Technol. 108 (1998) 114–120.

[3] R. Lima, B. Marple, Toward highly sintering-resistant nanostructured ZrO2–7 wt.% Y2O3 coatings for TBC applications by employing differential sintering, J. Therm. Spray Technol. 17 (2008) 846–852.
[4] R.L. Coble, Sintering crystalline solids. I. Intermediate and final state diffusion models, J. Appl. Phys. 32 (2004) 787–792.
[5] J. Thompson, T. Clyne, The effect of heat treatment on the stiffness of zirconia top coats in plasma-sprayed TBCs, Acta Mater. 49 (2001) 1565–1575.
[6] F. Cernuschi, L. Lorenzoni, S. Ahmaniemi, P. Vuoristo, T. Mäntylä, Studies of the sintering kinetics of thick thermal barrier coatings by thermal diffusivity measurements, J. Eur. Ceram. Soc. 25 (2005) 393–400.
[7] R. Krishnamurthy, D.J. Srolovitz, Sintering and microstructure evolution in columnar thermal barrier coatings, Acta Mater. 57 (2009) 1035–1048.
[8] F. Wakai, Y. Shinoda, T. Akatsu, Methods to calculate sintering stress of porous materials in equilibrium, Acta Mater. 52 (2004) 5621–5631.
[9] H. Riedel, H. Zipse, J. Svoboda, Equilibrium pore surfaces, sintering stresses and constitutive equations for the intermediate and late stages of sintering – II. Diffusional densification and creep, Acta Metall. Mater. 42 (1994) 445–452.
[10] B. Siebert, C. Funke, R. Vaβen, D. Stöver, Changes in porosity and Young's Modulus due to sintering of plasma sprayed thermal barrier coatings, J. Mater. Process. Technol. 92 (1999) 217–223.
[11] D. Zhu, R.A. Miller, Thermal conductivity and elastic modulus evolution of thermal barrier coatings under high heat flux conditions, J. Therm. Spray Technol. 9 (2000) 175–180.
[12] S. Paul, A. Cipitria, I. Golosnoy, L. Xie, M. Dorfman, T. Clyne, Effects of impurity content on the sintering characteristics of plasma-sprayed zirconia, J. Therm. Spray Technol. 16 (2007) 798–803.
[13] M. Ahrens, R. Vaßen, D. Stöver, S. Lampenscherf, Sintering and creep processes in plasma-sprayed thermal barrier coatings, J. Therm. Spray Technol. 13 (2004) 432–442.
[14] A. Cipitria, I.O. Golosnoy, T.W. Clyne, A sintering model for plasma-sprayed zirconia TBCs. Part I: free-standing coatings, Acta Mater. 57 (2009) 980–992.
[15] A. Cipitria, I.O. Golosnoy, T.W. Clyne, A sintering model for plasma-sprayed zirconia thermal barrier coatings. Part II: coatings bonded to a rigid substrate, Acta Mater. 57 (2009) 993–1003.
[16] A.C.F. Cocks, N.A. Fleck, Constrained sintering of an air-plasma-sprayed thermal barrier coating, Acta Mater. 58 (2010) 4233–4244.
[17] A. Cocks, N. Fleck, S. Lampenscherf, A brick model for asperity sintering and creep of APS TBCs, J. Mech. Phys. Solids 63 (2014) 412–431.
[18] Y. Li, C.J. Li, Q. Zhang, G.J. Yang, C.X. Li, Influence of TGO composition on the thermal shock lifetime of thermal barrier coatings with cold-sprayed MCrAlY bond coat, J. Therm. Spray Technol. 19 (2010) 168–177.
[19] Y. Bai, C. Ding, H. Li, Z. Han, B. Ding, T.J. Wang, L. Yu, Isothermal oxidation behavior of supersonic atmospheric plasma-sprayed thermal barrier coating system, J. Therm. Spray Technol. 22 (2013) 1201–1209.
[20] C.G. Levi, E. Sommer, S.G. Terry, A. Catanoiu, M. Rühle, Alumina grown during deposition of thermal barrier coatings on NiCrAlY, J. Am. Ceram. Soc. 86 (2003) 676–685.
[21] R. Xu, X. Fan, W. Zhang, Y. Song, T.J. Wang, Effects of geometrical and material parameters of top and bond coats on the interfacial fracture in thermal barrier coating system, Mater. Des. 47 (2013) 566–574.
[22] A.M. Karlsson, A. Evans, A numerical model for the cyclic instability of thermally grown oxides in thermal barrier systems, Acta Mater. 49 (2001) 1793–1804.
[23] W. Chen, X. Wu, B.R. Marple, D. Nagy, P. Patnaik, TGO growth behaviour in TBCs with APS and HVOF bond coats, Surf. Coat. Technol. 202 (2008) 2677–2683.
[24] A. Rabiei, A. Evans, Failure mechanisms associated with the thermally grown oxide in plasma-sprayed thermal barrier coatings, Acta Mater. 48 (2000) 3963–3976.
[25] M. Martena, D. Botto, P. Fino, S. Sabbadini, M. Gola, C. Badini, Modelling of TBC system failure: stress distribution as a function of TGO thickness and thermal expansion mismatch, Eng. Fail. Anal. 13 (2006) 409–426.
[26] M. Białas, Finite element analysis of stress distribution in thermal barrier coatings, Surf. Coat. Technol. 202 (2008) 6002–6010.
[27] W. Chen, X. Wu, B.R. Marple, P.C. Patnaik, Oxidation and crack nucleation/growth in an air-plasma-sprayed thermal barrier coating with NiCrAlY bond coat, Surf. Coat. Technol. 197 (2005) 109–115.
[28] R. Xu, X.L. Fan, W.X. Zhang, T.J. Wang, Interfacial fracture mechanism associated with mixed oxides growth in thermal barrier coating system, Surf. Coat. Technol. 253 (2014) 139–147.
[29] G.J. Yang, Z.L. Chen, C.X. Li, C.J. Li, Microstructural and mechanical property evolutions of plasma-sprayed YSZ coating during high-temperature exposure: Comparison study between 8YSZ and 20YSZ, J. Therm. Spray Technol. 22 (2013) 1294–1302.
[30] M. Danielsson, D. Parks, M. Boyce, Three-dimensional micromechanical modeling of voided polymeric materials, J. Mech. Phys. Solids 50 (2002) 351–379.
[31] M. Gasik, B. Zhang, A constitutive model and FE simulation for the sintering process of powder compacts, Comput. Mater. Sci. 18 (2000) 93–101.
[32] K. Shinagawa, Finite element simulation of sintering process: microscopic modelling of powder compacts and constitutive equation for sintering, JSME Int. J. Ser. A – Solid Mech. Mat. Eng. 39 (1996) 565–572.
[33] Q. Yu, A. Rauf, N. Wang, C. Zhou, Thermal properties of plasma-sprayed thermal barrier coating with bimodal structure, Ceram. Int. 37 (2011) 1093–1099.
[34] V. Lughi, V.K. Tolpygo, D.R. Clarke, Microstructural aspects of the sintering of thermal barrier coatings, Mater. Sci. Eng. A – Struct. Mater. Prop. Microstruct. Process. 368 (2004) 212–221.
[35] R. Vaßen, S. Giesen, D. Stöver, Lifetime of plasma-sprayed thermal barrier coatings: comparison of numerical and experimental results, J. Therm. Spray Technol. 18 (2009) 835–845.
[36] F. Cernuschi, I. Golosnoy, P. Bison, A. Moscatelli, R. Vassen, H.P. Bossmann, S. Capelli, Microstructural characterization of porous thermal barrier coatings by IR gas porosimetry and sintering forecasts, Acta Mater. 61 (2013) 248–262.
[37] N. Balasubramanian, T.G. Langdon, Flow processes in superplastic yttria-stabilized zirconia: a deformation limit diagram, Mater. Sci. Eng. A – Struct. Mater. Prop. Microstruct. Process. 409 (2005) 46–51.
[38] J. Zhang, V. Desai, Evaluation of thickness, porosity and pore shape of plasma sprayed TBC by electrochemical impedance spectroscopy, Surf. Coat. Technol. 190 (2005) 98–109.
[39] W.X. Zhang, X.L. Fan, T.J. Wang, The surface cracking behavior in air plasma sprayed thermal barrier coating system incorporating interface roughness effect, Appl. Surf. Sci. 258 (2011) 811–817.
[40] W.X. Zhang, T.J. Wang, L.X. Li, Numerical analysis of the transverse strengthening behavior of fiber-reinforced metal matrix composites, Comput. Mater. Sci. 39 (2007) 684–696.
[41] ABAQUS User's Manual, Dassault Systèmes Simulia Corporation, 2009.
[42] X. Zhao, X. Wang, P. Xiao, Sintering and failure behaviour of EB-PVD thermal barrier coating after isothermal treatment, Surf. Coat. Technol. 200 (2006) 5946–5955.
[43] S.R. Choi, D. Zhu, R.A. Miller, Effect of sintering on mechanical properties of plasma-sprayed zirconia-based thermal barrier coatings, J. Am. Ceram. Soc. 88 (2005) 2859–2867.
[44] E. Busso, J. Lin, S. Sakurai, M. Nakayama, A mechanistic study of oxidation-induced degradation in a plasma-sprayed thermal barrier coating system: Part I: model formulation, Acta Mater. 49 (2001) 1515–1528.